

Direct multiangle solution for poorly stratified atmospheres

Vladimir Kovalev,* Cyle Wold, Alexander Petkov, and Wei Min Hao

Forest Service, U.S. Department of Agriculture, Fire Sciences Laboratory, 5775 Hwy 10 West, Missoula, Montana 59808, USA

*Corresponding author: vkovalev@fs.fed.us

Received 12 December 2011; revised 19 June 2012; accepted 9 August 2012;
posted 10 August 2012 (Doc. ID 159792); published 29 August 2012

The direct multiangle solution is considered, which allows improving the scanning lidar-data-inversion accuracy when the requirement of the horizontally stratified atmosphere is poorly met. The signal measured at zenith or close to zenith is used as a core source for extracting optical characteristics of the atmospheric aerosol loading. The multiangle signals are used as auxiliary data to extract the vertical transmittance profile from the zenith signal. Details of the retrieval methodology are considered that eliminate, or at least soften, some specific ambiguities in the multiangle measurements in horizontally heterogeneous atmospheres. Simulated and experimental elastic lidar data are presented that illustrate the essentials of the data-processing technique. Finally, the prospects of the utilization of high-spectral-resolution lidar in the multiangle mode are discussed. © 2012 Optical Society of America

OCIS codes: 280.3640, 290.1350, 290.2200.

1. Introduction

The commonly used methodologies of multiangle measurements are mostly based on the assumption of horizontal stratification of the searched atmosphere. This rigid requirement [1,2], which significantly impedes the use of the methods in practice, is considered the main issue for the multiangle measurements. There have been some attempts to overcome this impediment and find simple and practical lidar-data-retrieval methods for the atmospheres where the above requirement is not rigidly met [3–6]. However, these and similar case studies include the same implicit assumptions as in the pioneer studies by Kano [1] and Hamilton [2]. These implicit assumptions contain two common points: (1) the spatial variations of the aerosol horizontal structure in the atmosphere obey some statistical “rules of the game,” particularly, obey some normal distribution; and (2) the backscatter signals used for the inversion are precisely determined, that is, no systematic (multiplicative or additive) distortions

in these exist over the whole measurement range; the retrieval accuracy depends only on the signal random noise.

Meanwhile, such an ideal picture is not realistic: the atmospheric structure does not obey any statistical laws, and nonzero additive and multiplicative distortions in lidar signals always take place. Our long-term investigations [7,8] revealed that even small distortions of the lidar signal, especially additive, may have an extremely destructive influence on the accuracy of the measurement results, and ignoring these may yield the wrong conclusion and recommendation.

Our methodology of multiangle data processing, developed in 2007 and based on simultaneously using both parameters in the Kano–Hamilton solution [9,10], allows some minimization of the influence of the systematic distortions in the inverted lidar signal on the retrieval results, especially over distant ranges. Using this basic principle, a practical methodology was developed that allowed computing the two-way transmission and the corresponding extinction coefficient profile in any slope direction searched during scanning [11].

In this paper we consider essentials and important details of the retrieval technique when the direct multiangle solution is used, that is, when the two-way transmission and the corresponding extinction coefficient are retrieved directly from the zenith signal. In our opinion, this relatively simple variant may be considered an optimal multiangle solution for poorly stratified atmospheres. We believe that the direct multiangle solution will nicely demonstrate its real value in the very near future, particularly when high-spectral-resolution lidars (HSRLs) are utilized in the multiangle mode. Taking into consideration the progress in HSRL technique and methodologies [12–15], one can expect significant progress in the multiangle measurements also.

2. Essentials of Direct Multiangle Solution

The direct multiangle solution is based on a combination of the one-directional and multiangle retrieval principles. The usual scanning procedure is performed, but now the backscatter signal measured at zenith (or close to the zenith direction) is a basic function for determining the vertical transmittance and the corresponding extinction coefficient profile. Unlike the conventional one-directional method, the direct multiangle solution uses the multiangle signals as the source of the auxiliary information for inverting the zenith signal. This auxiliary information allows avoiding the measurement uncertainty related with the unknown lidar ratio and the lidar constant inherent to vertically pointed elastic lidar.

The square-range-corrected backscatter signal, $P_{90}(h)h^2$, at the height h measured at zenith is the product of the lidar solution constant C , the total (molecular and particulate) vertical backscatter coefficient $\beta_{\pi,90}(h)$, and the total two-way vertical transmittance, $T_{90}^2(0, h)$, from ground level to the height h , that is,

$$P_{90}(h)h^2 = C\beta_{\pi,90}(h)T_{90}^2(0, h). \quad (1)$$

The two-way vertical transmittance,

$$T_{90}^2(0, h) = \exp[-2\tau_{90}(0, h)], \quad (2)$$

and the corresponding total vertical optical depth, $\tau_{90}(0, h)$, are generally the basic functions of interest to be determined. In the method under consideration, the two-way vertical transmittance $T_{90}^2(0, h)$ is determined from Eq. (1) as

$$T_{90}^2(0, h) = P_{90}(h)h^2 / \langle C\beta_{\pi,90}(h) \rangle, \quad (3)$$

where the estimate of the actual profile, $C\beta_{\pi,90}(h)$, symbolized here as $\langle C\beta_{\pi,90}(h) \rangle$, is found from the set of the multiangle signals, $P_i(h)$, measured by the same lidar under different elevation angles φ_i . As in the Kano–Hamilton method, the data points $y_i(h)$ are calculated from the logarithms of the square-range-corrected signals in the form

$$y_i(h) = \ln[P_i(h)(h/\sin \varphi_i)^2]. \quad (4)$$

The linear fit $\langle y(h) \rangle$ for the set of the data points $y_i(h)$ at the height h can be found in a general form as

$$\langle y(h) \rangle = \langle A(h) \rangle + b(h)x, \quad (5)$$

where $x = 1/\sin \varphi_i$ is the discrete variable, $b(h)$ is the slope of the linear fit, and the intercept $\langle A(h) \rangle$ is found by the extrapolation of the linear fit $\langle y(h) \rangle$ to $x = 0$. In the direct multiangle solution, the linear fit $\langle y(h) \rangle$ is shifted into the point $y_{90}(h)$, which is calculated as the logarithm of the zenith signal at the height h ; that is,

$$y_{90}(h) = \ln[P_{90}(h)h^2]. \quad (6)$$

Accordingly, the intercept $\langle A(h) \rangle$ is shifted into the point $A'(h)$, which can be determined as

$$A'(h) = y_{90}(h) - b(h). \quad (7)$$

The parameter of interest, $\langle C\beta_{\pi,90}(h) \rangle$, is determined as the exponent of the intercept, that is,

$$\langle C\beta_{\pi,90}(h) \rangle = \exp[A'(h)]. \quad (8)$$

To clarify the specifics of the above technique, let us perform numerical experiments for an artificial scanning lidar, which scans a poorly stratified synthetic atmosphere under nine elevation angles, 12°, 15°, 18°, 24°, 30°, 40°, 55°, 70°, and 90°. The arbitrarily selected data points of $C\beta_{\pi,\varphi}(h)$ and $\tau_{\varphi}(0, h)$ for the above nine angles φ_i at a height of interest h are shown in Fig. 1 as the filled squares and filled triangles, respectively. The empty triangles are the values of the vertical optical depths determined as the product of the corresponding slope optical depths, $\tau_{\varphi}(0, h)$, by $\sin \varphi_i$. One can see that this synthetic atmosphere is not stratified horizontally. The corresponding data points $y_i(h)$ (the filled circles) and

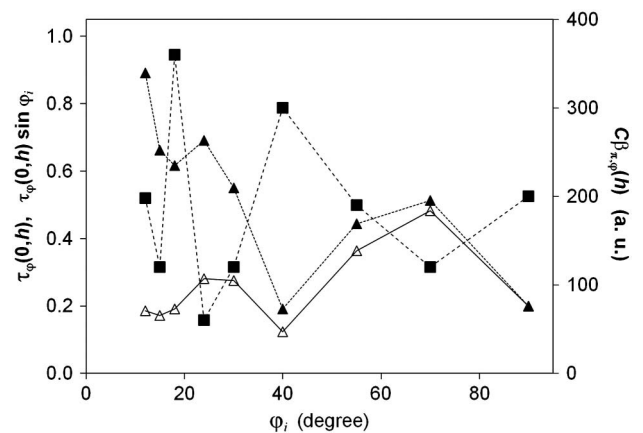


Fig. 1. Data points $C\beta_{\pi,\varphi}(h)$ (filled squares), $\tau_{\varphi}(0, h)$ (filled triangles), and $\tau_{\varphi}(0, h)\sin \varphi_i$ (empty triangles) versus the elevation angle φ_i for the angles selected for the numerical experiment.

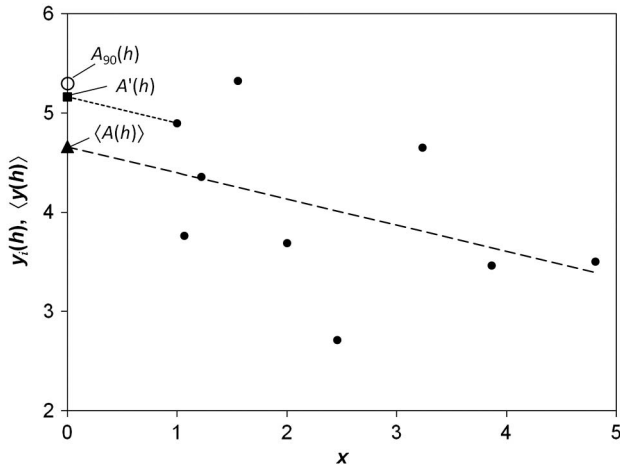


Fig. 2. Dependence of the data points $y_i(h)$ (filled circles) and the linear fit $\langle y(h) \rangle$ (dashed line) on $x = 1/\sin \varphi_i$. The actual intercept $A_{90}(h)$ for the zenith direction is shown on the y axis as the empty circle. The intercept points of the linear fit, $\langle A(h) \rangle$ and $A'(h)$, are shown as the filled triangle and the filled square, respectively.

the original linear fit $\langle y(h) \rangle$ (the dashed line) versus the independent $x = [\sin \varphi_i]^{-1}$ obtained with Eq. (5) are shown in Fig. 2. The interception point of the linear fit, obtained by the extrapolation of the linear fit into $x = 0$, is $\langle A(h) \rangle = 4.66$; it is shown on the vertical axis as the filled triangle. The corresponding exponent is $\langle C\beta_{\pi,90}(h) \rangle = \exp\langle A(h) \rangle = 105.6$ a.u. Meanwhile, the actual, that is, model values used for the simulations are $A_{90}(h) = 5.30$ (the empty circle), and $C\beta_{\pi,90}(h) = 200$ a.u.. Thus, when using the original $\langle A(h) \rangle$, the corresponding error of the estimate of the actual product $C\beta_{\pi,90}(h)$ is $\sim 47\%$.

The use of the direct multiangle solution, that is the determination of the intercept with Eq. (7), significantly decreases this error, putting the shifted data point $A'(h)$ (the filled square) closer to the actual point, $A_{90}(h)$. The use of the intersection point $A'(h)$ instead of initial $\langle A(h) \rangle$ reduces the corresponding error in the estimate, $\langle C\beta_{\pi,90}(h) \rangle$, down to $\sim 13\%$. Note that, in spite of the poor horizontal stratification of the atmosphere, the relative difference between $\langle C\beta_{\pi,90}(h) \rangle$ and actual $C\beta_{\pi,90}(h)$ is not so large as the difference between the actual optical depth, $\tau_{90}(0, h)$, and that retrieved from the slope $b(h)$ of the linear fit in Fig. 2. Indeed, $b(h) = -0.26$, that is, the corresponding vertical optical depth is $\langle \tau_{90}(0, h) \rangle = 0.13$; meanwhile, the true (model) value is $\tau_{90}(0, h) = 0.2$. That is, the difference between these is $\sim 35\%$.

Our analyses showed that in many cases the shifted point $A'(h)$ is closer to the actual location of the point, $A_{90}(h)$, than the initial data point $\langle A(h) \rangle$ found from Eq. (5). Such a shift of the linear fit into the point $y_{90}(h)$ is quite helpful when the data points $y_i(h)$ are strongly scattered and the point $y_{90}(h)$ at $x = 1$ is significantly shifted from the linear fit $\langle y(h) \rangle$.

Let us determine the retrieval uncertainty inherent to the direct multiangle solution. Simple

transformations yield the following formula for the ratio of the estimated $\langle C\beta_{\pi,90}(h) \rangle$ and the actual $C\beta_{\pi,90}(h)$,

$$\frac{\langle C\beta_{\pi,90}(h) \rangle}{C\beta_{\pi,90}(h)} = \exp[-2\tau_{90}(0, h) - b(h)]. \quad (9)$$

Accordingly, the corresponding relative error of the derived two-way vertical transmittance profile is

$$\delta[T_{90}^2(0, h)] = \exp[-2\tau_{90}(0, h) - b(h)] - 1. \quad (10)$$

As follows from Eqs. (9) and (10), the relative error in the estimated profile $\langle C\beta_{\pi,90}(h) \rangle$, and accordingly in the retrieved profile $T_{90}^2(0, h)$, depends only on the difference between the slope $b(h)$ and the actual doubled vertical optical depth in the zenith signal, $P_{90}(h)h^2$.

Let us return to the numerical simulations, considering the worst case of horizontal heterogeneity when the retrieval of the optical depth from the slope of the linear fit is impossible. In spite of the strong inhomogeneity of the optical parameters shown in Fig. 1, the slope b in Fig. 2 is still negative. In some cases of a poorly stratified aerosol atmosphere, the retrieved slope $b(h)$ may be positive or zero, that is, obviously erroneous. Such a situation when the slope $b(h)$ is positive and $\langle y(h) \rangle$ increases with the increase of x is illustrated by Figs. 3 and 4. The optical depth extracted from the slope of the linear fit in Fig. 4 is negative, $\langle \tau_{90}(0, h) \rangle = -0.026$. Accordingly, an unphysical negative extinction coefficient would be retrieved from such an erroneous optical depth. In this case, the use of Eq. (7) would yield $A'(h) = 4.52$ instead of the true $A_{90}(h) = 4.87$ (Fig. 4), and the extracted $\langle C\beta_{\pi,90}(h) \rangle$ would differ by $\sim 30\%$ from the true $C\beta_{\pi,90}(h)$.

To reduce such large errors in the estimated $\langle A(h) \rangle$ and $\langle C\beta_{\pi,90}(h) \rangle$ when the retrieved slope $b(h)$ is obviously erroneous, an additional correction procedure may be recommended. The intercept in such cases can be extracted more accurately, especially if the vertical optical depth can be somehow

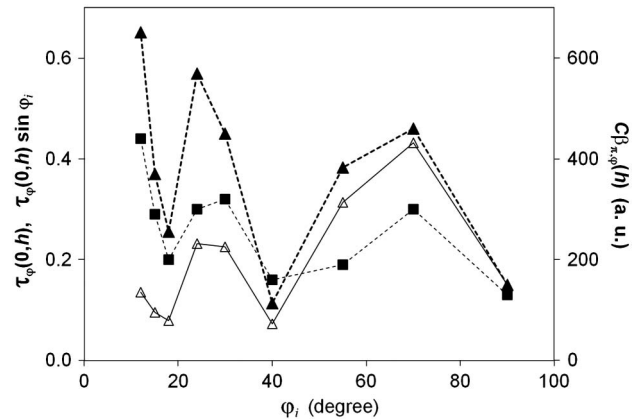


Fig. 3. Dependencies of the data points on x used for the second numerical experiment. The symbols are the same as in Fig. 1.

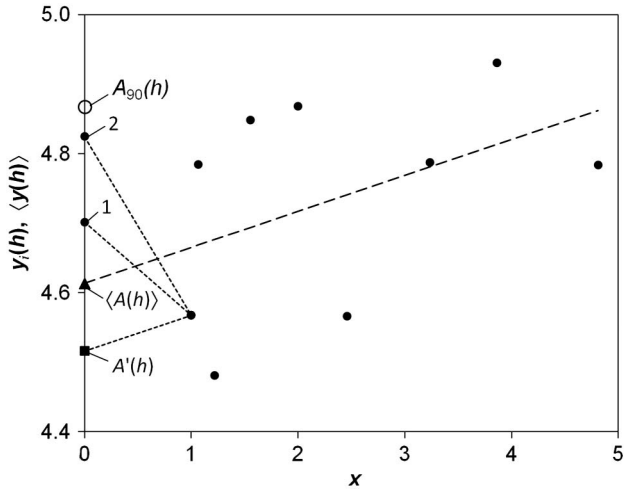


Fig. 4. Dependencies of the data points on x used for the second numerical experiment. The symbols are the same as in Fig. 1. The data points shown in Fig. 3 are used and $b(h)$ is replaced by $b_{\text{mol}}(h)$.

estimated. If not, one can achieve a sensible inversion result by using a minimal but realistic negative slope. In clear atmospheres, the purely molecular atmosphere can be assumed and the correction may be done by replacing the erroneous positive $b(h)$ by $b_{\text{mol}}(h)$, determined as

$$b_{\text{mol}}(h) = -2 \int_0^h \kappa_m(h') dh', \quad (11)$$

where $\kappa_m(h)$ is the molecular extinction coefficient at the height h . In other words, at any height where $b(h) > b_{\text{mol}}(h)$, the latter should be used instead of $b(h)$. The replacement of the erroneous $b(h)$ by $b_{\text{mol}}(h)$ for the case shown in Figs. 3 and 4 would yield $A'(h) = 4.70$ for $h = 1000$ m and $A'(h) = 4.82$ for $h = 2000$ m (points 1 and 2 in Fig. 4), significantly decreasing the relative error in the extracted $\langle C\beta_{\pi,90}(h) \rangle$. Obviously, such an operation is effective in the atmospheres where the aerosol loading is small. Otherwise, additional smoothing operations considered below are required.

3. Discussion

A. Ambiguity in Selection of Maximum Range of Inverted Lidar Signals in Multiangle Mode

To clarify the specifics of the conventional and the direct multiangle solutions, let us analyze the real experimental data obtained with the Missoula Fire Sciences Laboratory lidar on 28 August 2009. The scanning elastic lidar operates at two wavelengths, 355 nm and 1064 nm. For our current task, only data at 355 nm are considered. The emitted energy of the Nd:YAG laser at this wavelength is ~ 45 mJ, the light pulse duration ~ 10 ns. The receiver section of the lidar consists of a 25 cm Schmidt–Cassegrain telescope and a photomultiplier. The lidar scan range is 0° to 180° in azimuth and 0° to 90° in elevation. The lidar measurements were performed in the

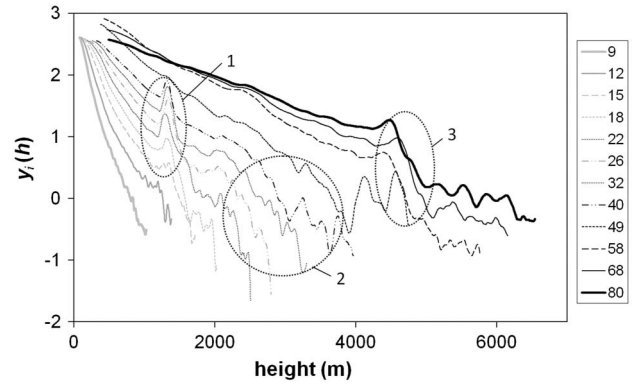


Fig. 5. Logarithms of the square-range-corrected signals versus height for 12 elevation angles retrieved from the lidar data at 355 nm in a smoke-polluted atmosphere on 28 August 2009. The height intervals for the signals shown in the figure are taken arbitrarily to provide better visualization of the specifics of the functions $y_i(h)$ in the searched atmosphere.

vicinity of wildfires where the atmospheric inversion created multiple smoke layers at different heights. To reduce the influence of local atmospheric horizontal heterogeneity, combined azimuthal–vertical searching [16] was conducted. This azimuthal scanning was made along 12 elevation angles, 9° , 12° , 15° , 18° , 22° , 26° , 32° , 40° , 49° , 58° , 68° , and 80° , the integration time for single angle profile was approximately 1 min.

For each elevation angle, a mean azimuthal signal and its logarithm were calculated and then used for the inversion. In Fig. 5, the logarithms of the mean azimuthal signals for the selected elevation angles are shown. The multilayered atmospheric structure is clearly seen over three zones, 1, 2, and 3, located at the heights 1000 to 1500 m, 2000 to 3500 m, and 4300 to 4700 m, respectively.

Following the common retrieval procedures, the linear fits $\langle y(h) \rangle$ for the data points $y_i(h)$ [Eq. (4)] were initially found for the discrete heights, from the minimum height h_{min} up to the maximum height h_{max} ; that is, $y_i(h)$ are determined for the heights $h_{\text{min}}, h_{\text{min}} + \Delta h, h_{\text{min}} + 2\Delta h, h_{\text{min}} + 3\Delta h, \dots, h_{\text{min}} + n\Delta h, \dots, h_{\text{max}}$. In the considered case, the height resolution was $\Delta h = 1.5$ m.

To determine the parameters of the linear fits $\langle y(h) \rangle$, the operative range $r_{\text{min}} - r_{\text{max}}$ of the inverted signals, and accordingly the range of the inverted functions $y_i(h)$, should be established. The minimal range, r_{min} , is generally selected somewhere outside and close to the incomplete overlap zone. The selection of the maximal range, r_{max} , is not so straightforward. Typically, the level of the random noise is considered as the main factor for selecting the maximum range [17–19], and some arbitrarily selected level of the signal-to-noise ratio is taken as the criterion for the selection of r_{max} .

The use of the signal-to-noise ratio as an only criterion is not the best option; for the real backscatter signals with nonzero additive distortion, determined in real, not perfectly stratified atmospheres, the

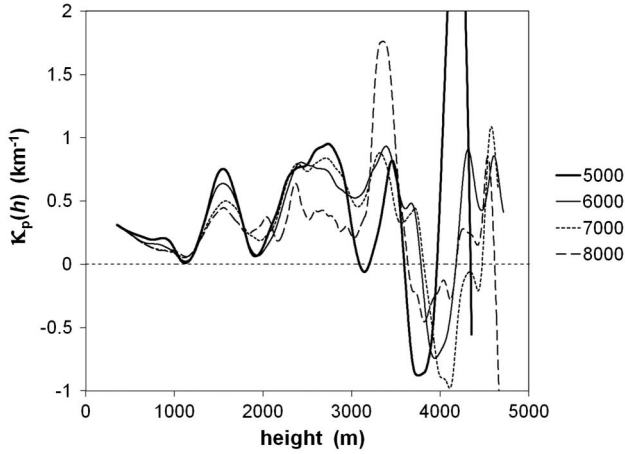


Fig. 6. Particulate extinction coefficient profiles, extracted from the functions $y_i(h)$ shown in Fig. 5 with the sliding range resolution of 300 m using the conventional Kano–Hamilton retrieval procedure. The values of r_{\max} in meters selected for the inversion are shown in the legend.

slope of the linear fit ($y(h)$) may strongly depend on such an arbitrarily selected r_{\max} . Unfortunately, no theory exists that would give practical recommendations for determining r_{\max} in such conditions. The only way to clarify this issue is through experiment; that is, it can be done by analyzing the inversion results obtained with different r_{\max} . Unfortunately, the use of this general idea in the conventional Kano–Hamilton inversion method yields discouraging results. The particulate extinction coefficient profiles, $\kappa_p(h)$, obtained with this method from the curves in Fig. 5 using different r_{\max} are shown in Fig. 6. These profiles are extracted from the optical depth profiles with the sliding derivative over the interval 300 m where the optical depth profiles were initially averaged within the height intervals of 300 m. One can see that these $\kappa_p(h)$ profiles, extracted from the same set of signals but using different r_{\max} , significantly differ each from other at the heights $h > 1200$ m. Obviously, this issue, the ambiguity in the selection of an optimal maximum range, should be somehow overcome. The retrieval procedures used in the direct multiangle solution allow solving this issue.

B. Direct Multiangle Solution: Retrieval Procedure

Let us consider the retrieval methodology in detail. The first step in the retrieval is establishing some set of the sensible discrete ranges, $r_{\max,1}, r_{\max,2}, \dots, r_{\max,j}, \dots, r_{\max,N}$, and calculating the corresponding number of the profiles of $A'(h)$ and $\langle C\beta_{\pi,90}(h) \rangle = \exp A'(h)$. For the case under consideration, the sensible ranges of r_{\max} were selected within the distances from $r_{\max,1} = 4000$ m to $r_{\max,N} = 10,000$ m; the discrete values of $r_{\max,j}$ are selected with the interval 1000 m between these. For simplicity, the same minimum range, $r_{\min} = 500$ m, is used in all cases.

For each selected range, $r_{\min} - r_{j,\max}$, the retrieved data undergo the following procedures:

(1) The profiles of $A'(h)$ and $b(h)$ [Eq. (7)] versus height are determined within the altitude range, $h_{\min} - h_{j,\max}$. For the altitudes where $b(h)$ proved to be less than $b_{\text{mol}}(h)$, it is replaced by $b_{\text{mol}}(h)$ found with Eq. (11).

(2) In case of large scattering of the initial data points $y_i(h)$, an additional shaping of the functions $b(h)$ may be required to eliminate possible erroneous local increase of the slope $b(h)$ with height. In our case, the profile $b(h)$ is smoothed using the 300 m sliding average; then it is transformed into the function $b'(h)$, which is found with the formula

$$b'(h) = \min[b(h_{\min}), b(h_{\min} + \Delta h), \dots, b(h - \Delta h), b(h)]. \quad (12)$$

(3) The function $b'(h)$ is used to recalculate the corresponding profile $A'(h)$. In our case, the maximal elevation angle was 80° , so that $x_{\min} > 1$; therefore, the profile $A'(h)$ was recalculated using the more general form of the formula in Eq. (7),

$$A'(h) = y(h, x_{\min}) - b'(h)x_{\min}. \quad (13)$$

(4) To eliminate possible local increasing of the derived two-way zenith transmission profile with height, the profile $A'(h)$ is adjusted with the formula

$$A'_{\text{adj}}(h) = \max[A'(h_{\min}), A'(h_{\min} + \Delta h), \dots, A'(h - \Delta h), h]. \quad (14)$$

(5) Using the adjusted profile $A'_{\text{adj}}(h)$, the corresponding two-way vertical transmission profile, $T_{90,p}^2(0, h)$, is obtained by removing the molecular component, $T_{80,m}^2(0, h)$:

$$T_{90,p}^2(0, h) = \left[\frac{T_{80}^2(0, h)}{T_{80,m}^2(0, h)} \right]^{(1/x_{\min})} = \left[\frac{P_{80}(h)(hx_{\min})^2}{T_{80,m}^2(0, h) \exp[A'_{\text{adj}}(h)]} \right]^{(1/x_{\min})}. \quad (15)$$

Operations (1) through (5) are repeated N times, selecting the corresponding discrete ranges, $r_{\max,1}, r_{\max,2}, \dots, r_{\max,N}$. When all N profiles of $T_{90,p}^2(0, h)$ are retrieved, their average, $T_{90,p,\text{aver}}^2(0, h)$, and the standard deviation, $\Delta T_{90,p}^2(h)$, are calculated. The acceptable boundaries of the average function $T_{90,p,\text{aver}}^2(0, h)$ are selected. The profiles $T_{90,p}^2(0, h)$ that extend significantly outside the area restricted by the boundaries $[T_{90,p,\text{aver}}^2(0, h) - \Delta T_{90,p}^2(h)]$ and $[T_{90,p,\text{aver}}^2(0, h) + \Delta T_{90,p}^2(h)]$ are excluded, and $T_{90,p,\text{aver}}^2(0, h)$ is recalculated. In the case under consideration, three profiles $T_{90,p}^2(0, h)$, determined with the marginal $r_{\max,j}$ equal to 4000, 9000, and 10,000 m, were excluded. After that the average for the remaining profiles

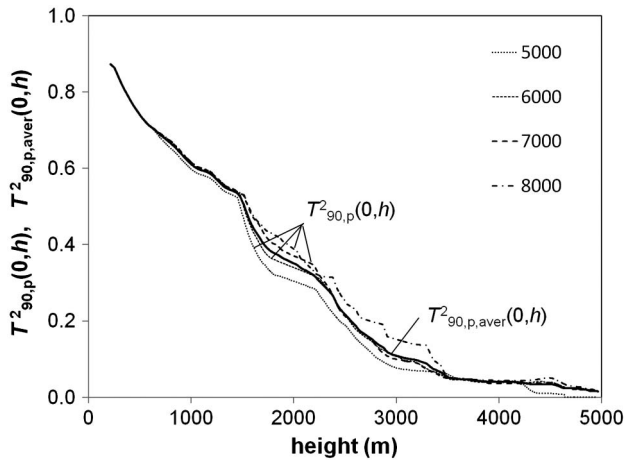


Fig. 7. Two-way vertical particulate transmission profiles, $T^2_{90,p}(0, h)$, extracted with Eq. (15) from the functions $y_i(h)$ in Fig. 5, and their average, $T^2_{90,p,aver}(0, h)$, obtained after excluding three marginal profiles.

$T^2_{90,p}(0, h)$ was calculated; the remaining individual profiles $T^2_{90,p}(0, h)$ and their average are shown in Fig. 7.

In Fig. 8, the bold curve represents the profile of the particulate extinction coefficient, $\kappa_p(h)$, extracted from the logarithm of $T^2_{90,p,aver}(0, h)$ using the sliding numerical derivative with the range resolution 300 m. Taking into consideration the specifics of the functions $y_i(h)$ in Fig. 5, one can conclude that the profile of the derived extinction coefficient in Fig. 8 looks sensible up to height ~ 5000 m. The location of the polluted layer above the height ~ 4500 m in Fig. 8 coincides with the sharp decrease in the intensity of the signals and the corresponding functions $y_i(h)$ in zone 3 (Fig. 5); this decrease is clearly seen in the basic profile, $y_{80}(h)$. For comparison, the profile of the extinction coefficient, extracted with the conventional Kano–Hamilton inversion method, is also shown in the figure (dotted curve). This

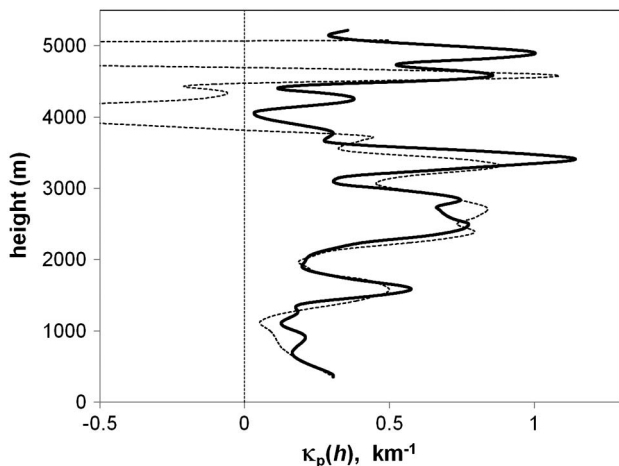


Fig. 8. Vertical profile of the particulate extinction coefficient extracted from the average profile $T^2_{90,p,aver}(0, h)$ shown in Fig. 7 (thick curve) and that extracted using the Kano–Hamilton solution with $r_{\max} = 7000$ m (dotted curve).

profile, extracted with $r_{\max} = 7000$ m, proved to be closest to that obtained with the direct solution method. Comparing these two profiles, one can see that they agree relatively closely to each other in the near zone up to the height ~ 3500 m but significantly diverge at higher altitudes. Thus, even the use of the optimal range, $r_{\max} = 7000$ m, in the Kano–Hamilton method does not provide the proper inversion results at high altitudes. The strong fluctuations of the profile $\kappa_p(h)$ derived with this method do not allow any estimation of the extinction coefficient behavior at heights higher than 3500 m. The improved inversion result obtained with the direct multiangle solution is due to the extraction of the information for the inversion directly from the signal $P_{80}(h)$, which over large distances is more accurate than the slope $b(h)$, retrieved with the conventional multiangle solution.

C. Specifics of Utilizing HSRL in Scanning Mode: Preliminary Analysis

In the recent study by Adam [20], the comparison of the backscatter and extinction coefficient profiles derived from the scanning elastic lidar data with the data of zenith-directed lidars was made. The author concluded that the multiangle retrieval methods proposed in [11] potentially are more accurate than the one-directional ones. This conclusion was made on the analysis of the multiangle measurements performed in an ideally stratified atmosphere. Obviously, no such ideal horizontally homogeneous atmosphere exists. However, the use of scanning HSRL, for which the atmosphere is much better horizontally stratified than for elastic lidar, may significantly improve the accuracy of the multiangle method.

Let us consider applying the direct multiangle solution to the molecular channel of the scanning HSRL. Following [14], the range-corrected signal in the molecular channel of HSRL in the slope direction φ can be defined as a function of height in the form

$$\frac{P_m(h)h^2}{\sin^2 \varphi} = C_m \frac{\Delta h}{\sin \varphi} f_m(T, p) \beta_{\pi, m}(h) \times \exp\{-2[\tau_{m, \varphi}(0, h) + \tau_{p, \varphi}(0, h)]\}, \quad (16)$$

where $P_m(h)$ is the signal in the molecular channel at the height h , C_m is a constant, $\Delta h / \sin \varphi$ is the range resolution, $\beta_{\pi, m}(h)$ is the molecular backscatter coefficient, $f_m(T, p)$ is a molecular temperature- and pressure-dependent factor, and $\tau_{m, \varphi}(0, h)$ and $\tau_{p, \varphi}(0, h)$ are the molecular and particulate optical depths within the layer $(0, h)$ in the slope direction φ . The function $f_m(T, p)$ is the most critical height-dependent Cabannes–Brillouin scattering spectrum function, which depends on the air temperature T and pressure p on the height h and needs to be transformed into the height-dependent function.

The logarithm of the function in Eq. (16) may be written in the form

$$\ln \left[\frac{P_m(h)h^2}{\sin \varphi} \right] = A_m(h) - \frac{2}{\sin \varphi} [\tau_{m,90}(0, h) + \tau_{p,90}(0, h)], \quad (17)$$

where

$$A_m(h) = \ln \left[C_m \frac{\Delta h}{\sin \varphi} f_m(T, p) \beta_{\pi, m}(h) \right], \quad (18)$$

and $\tau_{m,90}(0, h)$ and $\tau_{p,90}(0, h)$ are the molecular and aerosol optical depths of the layer $(0, h)$ in the vertical direction.

As in the elastic lidar measurements, the linear fit for the data points in Eq. (17), obtained in different slope directions, is found, and its slope and the interception points are determined. However, unlike the elastic lidar, the term $A_m(h)$ in Eq. (17) does not depend on the horizontal aerosol heterogeneity because the aerosol backscatter component in the molecular channel of HSRL is filtered out. This specific provides much more accurate inversion data. Moreover, the filtered transmitted backscattered spectrum, which has extremely complicated spectral shape and should be known in the case of the one-directional mode, now can be determined directly from the interception point of the linear fit. For illustration, in Fig. 9 the dependence of the data points $y_i(h)$ and the corresponding linear fit on $x = 1/\sin \varphi_i$ obtained from the synthetic HSRL is shown. The data are obtained for the same atmospheric conditions as shown in Fig. 3, but this time from the signals of the molecular channel of HSRL, where $A_m(h) = \text{constant}$ and only variations in the slope optical depths distort the measurement results. The comparison of Figs. 4 and 9 nicely demonstrates the potential advantages of HSRL as compared with elastic lidar.

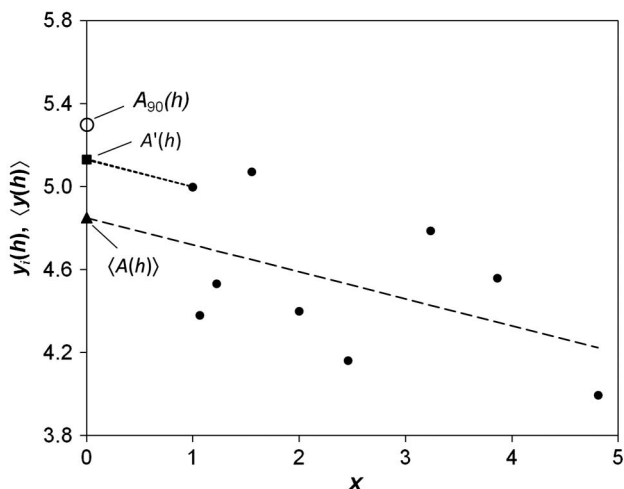


Fig. 9. Dependence of the data points $y_i(h)$ (filled circles) and the linear fit $\langle y(h) \rangle$ (dashed line) on x for the scanning HSRL, operating in the atmospheric conditions shown in Fig. 3.

4. Summary

The goal of this study was to discuss the direct multi-angle solution, a variant of the multiangle inversion methodology, which would be less sensitive both to poor stratification of the atmosphere and to the lidar signal distortions. To achieve this objective, the improved retrieval technique was developed in which the signal measured by the scanning lidar at zenith (or close to zenith) is used as the core source of information about the aerosol vertical profile. The set of multiangle signals extracted from the same lidar is used as the source of auxiliary information to extract the profile of the vertical transmittance from the zenith signal. To avoid an arbitrary selection of the maximal range of the inverted lidar signals, which may yield a casual rather than an optimal inversion result, the set of the two-way transmittance profiles is determined using different maximum ranges of the inverted backscatter signals. The average of these profiles and the corresponding standard deviation of the average are calculated and used to exclude from the final analysis the profiles that are significantly shifted from the average transmission profile.

The use of HSRL in multiangle mode allows excluding the requirement of the horizontal homogeneity of the aerosol backscattering. The only requirement that should be met is that the slant optical depths are proportional to $1/\sin \varphi$; this requirement can be easily controlled as the variations of the aerosol backscattering do not mask the distortions in the slant optical depths. The intersection points of the linear fit of the signal logarithms allow determining the relative backscattering function without using *a priori* assumptions about the Cabannes–Brillouin scattering spectrum.

References

1. M. Kano, "On the determination of backscattering and extinction coefficient of the atmosphere by using a laser radar," *Papers Meteorol. Geophys.* **19**, 121–129 (1968).
2. P. M. Hamilton, "Lidar measurement of backscatter and attenuation of atmospheric aerosol," *Atmos. Environ.* **3**, 221–223 (1969).
3. J. D. Spinhirne, J. A. Reagan, and B. M. Herman, "Vertical distribution of aerosol extinction cross section and inference of aerosol imaginary index in the troposphere by lidar technique," *J. Appl. Meteorol.* **19**, 426–438 (1980).
4. T. Takamura, Y. Sasano, and T. Hayasaka, "Tropospheric aerosol optical properties derived from lidar, sun photometer, and optical particle counter measurements," *Appl. Opt.* **33**, 7132–7140 (1994).
5. M. Sicard, P. Chazette, J. Pelon, J. G. Won, and S. Yoon, "Variational method for the retrieval of the optical thickness and the backscatter coefficient from multiangle lidar profiles," *Appl. Opt.* **41**, 493–502 (2002).
6. J. N. Porter, B. Lienert, and S. K. Sharma, "Using horizontal and slant lidar measurements to obtain calibrated aerosol scattering coefficients from a coastal lidar in Hawaii," *J. Atmos. Ocean. Technol.* **17**, 1445–1454 (2000).
7. V. A. Kovalev, "Distortion of the extinction-coefficient profiles caused by systematic distortions in lidar data," *Appl. Opt.* **43**, 3191–3198 (2004).
8. V. A. Kovalev, W. M. Hao, C. Wold, and M. Adam, "Experimental method for the examination of systematic distortions in lidar data," *Appl. Opt.* **46**, 6710–6718 (2007).

9. V. A. Kovalev, W. M. Hao, and C. Wold, "Determination of the particulate extinction-coefficient profile and the column-integrated lidar ratios using the backscatter-coefficient and optical-depth profiles," *Appl. Opt.* **46**, 8627–8634 (2007).
10. V. Kovalev, C. Wold, W. M. Hao, and B. Nordgren, "Improved methodology for the retrieval of the particulate extinction coefficient and lidar ratio from the lidar multiangle measurement," *Proc. SPIE* **6750**, 67501B (2007).
11. V. A. Kovalev, A. Petkov, C. Wold, and W. M. Hao, "Modified technique for processing multiangle lidar data measured in clear and moderately polluted atmospheres," *Appl. Opt.* **50**, 4957–4966 (2011).
12. M. Esselborn, M. Wirth, A. Fix, M. Tesche, and G. Ehret, "Airborne high spectral resolution lidar for measuring aerosol extinction and backscatter coefficients," *Appl. Opt.* **47**, 346–358 (2008).
13. J. W. Hair, C. A. Hostetler, A. L. Cook, D. B. Harper, R. A. Ferrare, T. L. Mack, W. Welch, L. R. Izquierdo, and F. E. Hovis, "Airborne high spectral resolution lidar for profiling aerosol optical properties," *Appl. Opt.* **47**, 6734–6752 (2008).
14. B. Liu, M. Esselborn, M. Wirth, A. Fix, D. Bi, and G. Ehret, "Influence of molecular scattering models on aerosol optical properties measured by high spectral resolution lidar," *Appl. Opt.* **48**, 5143–5154 (2009).
15. R. R. Rogers, C. A. Hostetler, J. W. Hair, R. A. Ferrare, Z. Liu, M. D. Obland, D. B. Harper, A. L. Cook, K. A. Powell, M. A. Vaughan, and D. M. Winker, "Assessment of the CALIPSO lidar 532 nm attenuated backscatter calibration using the NASA LaRC airborne high spectral resolution lidar," *Atmos. Chem. Phys.* **11**, 1295–1311 (2011).
16. M. Adam, V. Kovalev, C. Wold, J. Newton, M. Pahlow, W. M. Hao, and M. B. Parlange, "Application of the Kano–Hamilton multiangle inversion method in clear atmospheres," *J. Atmos. Ocean. Technol.* **24**, 2014–2028 (2007).
17. D. N. Whiteman, "Application of statistical methods to the determination of slope in lidar data," *Appl. Opt.* **38**, 3360–3369 (1999).
18. S. N. Volkov, B. V. Kaul, and D. I. Shefontuk, "Optimal method of linear regression in laser remote sensing," *Appl. Opt.* **41**, 5078–5083 (2002).
19. F. Rocadenbosch, A. Comeron, and D. Pineda, "Assessment of lidar inversion errors for homogeneous atmospheres," *Appl. Opt.* **37**, 2199–2206 (1998).
20. M. Adam, "Vertical versus scanning lidar measurements in horizontally homogeneous atmosphere," *Appl. Opt.* **51**, 4491–4500 (2012).